



# The effect of energy density and porosity structure on tensile properties of 316L stainless steel produced by laser powder bed fusion

Stefania Cacace<sup>1</sup> · Luca Pagani<sup>2</sup> · Bianca M. Colosimo<sup>1</sup> · Quirico Semeraro<sup>1</sup>

Received: 4 May 2021 / Accepted: 27 February 2022  
© The Author(s) 2022

## Abstract

Understanding the influence of process parameters and defect structure on the properties of parts produced via laser powder bed fusion (L-PBF) is a fundamental step towards the broader use of additive manufacturing technologies in critical applications. Furthermore, the ability to predict mechanical properties by simply considering information on the process parameters and defects observed via X-ray computer tomography (XCT) allows one to avoid expensive destructive testing, provide an in-depth understanding of the process quality and represents a viable solution towards process optimisation. Most of the previous works showed that energy density could be used as an excellent synthetic indicator to predict the mechanical properties of parts produced by L-PBF. This paper explores the effect of different energy density levels on the tensile properties of 316L stainless steel parts produced by L-PBF. Different from previous works in the literature, the same level of energy density is obtained considering various combinations of process parameters (speed, power and hatch distance). While energy density is shown to be a good synthetic indicator for predicting ultimate tensile strength (UTS) and yield strength (YS), a different behaviour is observed for elongation. Elongation shows a significant variability even when samples are produced at the same level of energy density, which contrasts with results obtained for UTS and YS. Synthetic indices representing the porosity structure are shown to be quite significant for predicting elongation even when the optimal energy density is considered. By combining process parameters with porosity structure, we show that almost a full prediction of the tensile properties can be achieved, paving the way for a significant reduction in expensive destructive tests.

**Keywords** Tensile tests · UTS · YS · Elongation · Porosity · Additive manufacturing · L-PBF · SLM · AISI 316L · X-ray computed tomography

## 1 Introduction

Laser powder bed fusion (L-PBF) technology has emerged as a new manufacturing candidate to produce critical parts in the automotive, aerospace and biomedical sectors. The advantages of this technology are well-known: weight reduction, geometric complexity for functionalised products and near net-shape production. However, the path towards a complete maturity of this technology is still challenged by internal defects, which appear to be typical of the process [1, 2].

Limiting the presence of defects in L-PBF parts is essential to ensure high mechanical properties. The mechanism of defect formation has been widely investigated in the literature. Simulation and analytical models [3, 4] as well as experimental campaigns [5, 6] were carried out to determine in which condition it is possible to obtain fully dense parts. For this purpose, process maps have been developed to identify the optimal process parameters (usually laser power and laser speed) with respect to the porosity content [7–10], even if defects can also occur when optimal process conditions are assumed [11].

The concept of a process map linking porosity to process parameters can be further simplified considering a synthetic index known as energy density, which is used to summarise the energy level per unit volume considered during layer melting. In particular, the volumetric energy density VED ( $J/mm^3$ ) for a pulsed laser is defined as:

✉ Stefania Cacace  
stefania.cacace@polimi.it

<sup>1</sup> Dipartimento di Meccanica, Politecnico di Milano, Via La Masa 1, 20156 Milano, Italy

<sup>2</sup> EPSRC Future Metrology Hub, University of Huddersfield, Huddersfield HD13DH, Queensgate, UK

$$E_d = \frac{P \cdot t}{d_p \cdot d_h \cdot z} \quad (1)$$

where  $P$  (W) is the laser power,  $t$  ( $\mu\text{s}$ ) is the exposure time,  $d_p$  ( $\mu\text{m}$ ) is the point distance,  $d_h$  ( $\mu\text{m}$ ) is the hatch distance and  $z$  ( $\mu\text{m}$ ) is the layer thickness.

Low-energy values result in a lack of fusion (LOF) porosity, which means that the energy is not sufficient to melt the powder fully, resulting in large irregular porosities spread all across the part [12]. High-energy density values result in over-melting, usually referred to as keyhole porosity [13]. At high-laser power and scan speed, the balling effect takes place [14, 15]. In this condition, the molten track breaks into droplets and it does not solidify uniformly, generating defects in the final part. In the region between these energy density limits, the steady region is used to denote the range of values ensuring the complete melting of the track and bonding between adjacent layers.

Different authors [16, 17] showed that parts with the same static properties can be printed using a small range of process parameters ( $\pm 10\%$ ) and values of the energy densities in the steady region. Furthermore, according to these papers, the energy density alone can be used successfully to predict the mechanical properties of the parts despite changes in the process parameter settings determining the same energy density. In conclusion, it is a standard practice to assume that the mechanical properties of L-PBF parts can be predicted easily considering the energy density value only, without the need to specify the specific parameter setting.

This work investigates how tensile properties, namely UTS, YS and elongation, vary when a large range of energy densities are used, and different process parameter combinations are used to obtain the same level of energy density. The experimental results show that while the energy density can predict UTS and YS, the *porosity structure*, defined as the distribution of volume, position and shape of the porosity inside the sample, plays an important role in predicting the elongation.

The porosity structure can be detected using XCT. The use of XCT to characterise the influence of the internal structure of L-PBF parts is well established in the literature [18–21], and [22]. Porosity in L-PBF can be divided into two main categories according to Snow et al. in [11]: the first is made of systematic flaws due to the suboptimal selection of process parameters. In contrast, the second class is represented by random flaws, which can be ascribed to random and unpredictable fluctuations in the quality of materials and processes, such as the natural variability of the powder feedstock, the irregular layering of particles and the random occurrence of atmospheric changes. The former group of defects can be avoided by selecting the appropriate energy density region, i.e., the steady region (Fig. 1), so as to avoid

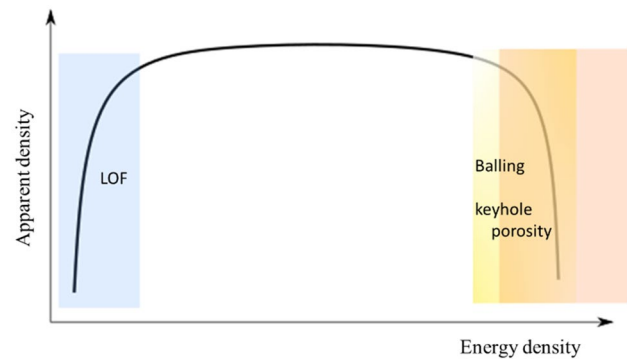


Fig. 1 Relationship between part density and energy density

keyhole porosity, balling and a lack of fusion conditions. On the other hand, random flaws cannot be predicted and can occur even when optimal process parameters are used.

Kim et al. [23] studied the porosity structure of Co-Cr disks produced via L-PBF using different combinations of process parameters, with different process settings determining the same energy density. In this work, speed and hatch distance were varied and, as a result, two energy density levels ( $30.5$  and  $60.9 \text{ J/mm}^3$ ) were obtained with two different combinations of process parameters each. According to this study, the mean density of samples sharing the same energy density was similar even if characterised by a different porosity structure measured via XCT.

The influence of porosity on the static properties of manufactured parts was also investigated in two recent papers. Yang et al. [24] studied the influence of linear energy density (evaluated as laser power divided by laser speed) and the VED on AISi10Mg samples produced via L-PBF, showing that the number of pores decreased as both the power and the scanning speed decreased. In their study, the authors provide information about the resulting tensile properties, but no statistical analysis of the correlation between pore structure and the mechanical performances was shown. In Salarian et al. [25], the pore structure of L-PBF specimens is correlated to their tensile behaviour using Inconel 625. The experiment entailed varying the laser power and keeping the other parameters fixed. They found that the pore morphology influenced strain to failure, but no statistical evidence is provided.

Zhang et al. [26] studied the relationship between porosity and the ductility of magnesium alloy in high-pressure die casting. The result showed that local porosity played a primary role in determining the elongation of the samples. Erickson et al. [27] used a finite element modelling method to simulate different porosity networks based on real data from additive manufacturing experiments. Tensile specimens were tested virtually, and the relationship between porosity and tensile properties was

investigated using a descriptor function that considered the volume and the position of pores. A summary of the literature on the influence of porosity structure on final part properties is reported in Table 1.

This paper explores the use of the VED as a unique indicator to predict UTS, YS and elongation of 316L stainless steel parts produced via L-PBF. A specific experimental campaign is carried out to show that the porosity structure can also be relevant to predict mechanical properties. In particular, the paper presents a new model, combining the VED with a few indicators representing the porosity structure as a viable solution to represent the tensile properties completely.

The paper is organised as follows. In Sect. 2, the experimental design and procedures are described. In Sect. 3.1, the results of the apparent density and tensile properties for all samples are described and discussed. A regression equation that predicts UTS based on the energy density is estimated. In Sect. 3.2, a fractographic and microstructural analysis of selected samples at a specific energy density value is carried out. In Sect. 4, the porosity structure is analysed qualitatively and quantitatively. In conclusion, a model predicting elongation based on the porosity index is presented.

## 2 Experimental procedures

### 2.1 L-PBF machine and material

Tensile test samples were produced using a L-PBF Renishaw AM250 system. The industrial machine is equipped with a Nd:YAG laser working in pulsed mode; the maximum power is 200 W and the laser spot diameter is 70  $\mu\text{m}$  at the focal position. The material used in this study was stainless steel powder 316L (LPW Technology Inc.), with a size range between 15 and 45  $\mu\text{m}$ , produced with the gas atomisation process (Fig. 2).

The chemical composition provided by the manufacturer is shown in Table 1, and it is compliant with AM standard ASTM F3184-16.

### 2.2 Process parameters

Process parameters were selected following the procedure described in [16]. The idea is to select different combinations of process parameters resulting in predefined values of energy density values. For the present work, samples were built at three levels of energy density: 59, 103 and 180  $\text{J}/\text{mm}^3$ . The smaller value, 59.2  $\text{J}/\text{mm}^3$ , belongs to the steady region of

**Table 1** Summary of the literature review

	Process	Number of samples	Material	Experimental design	Tensile tests	Result	Statistical analysis
Kim et al. [23]	L-PBF	6	CoCr	Scan speed, hatch distance varied. Same VED	No	Mean density similar, but different porosity structures	–
Yang et al. [24]	L-PBF	5 same VED, 5 same LED	AlSi10Mg	Power, speed, hatch distance varied. Same VED and LED	Yes	Higher power reduces porosity resulting in higher UTS	No
Salarian et al. [25]	L-PBF	4	Inconel 625	Power varied, other parameters were fixed	Yes	Pore morphology influences strain to failure	No
Zhang et al. [26]	High-pressure die casting	20	AM60	None	Yes	Maximum volume reduction is correlated with elongation	Yes
Erickson et al. [27]	L-PBF	120	17–4 PH	Same parameters	Yes (simulated data)	A porosity index based on pore position is correlated with fracture location	Yes
Present work	L-PBF	12	AISI 316L	Power, point distance, exposure time, hatch distance varied with the same VED	Yes	Maximum volume reduction is correlated with elongation	Yes

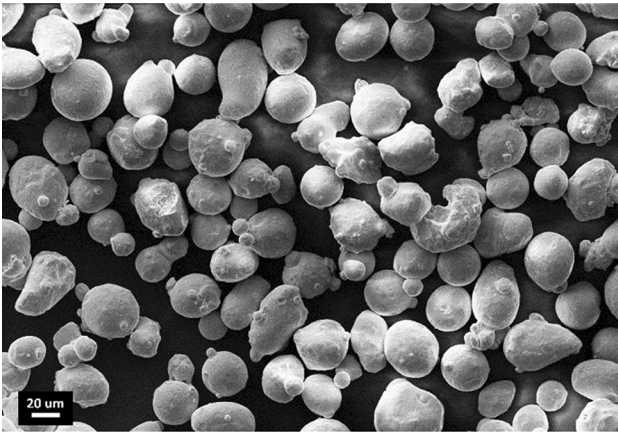


**Fig. 2** SEM image of AISI 316L powder

energy density as defined in Fig. 1, and it was selected based on our experience with the machine and a preliminary experimental campaign not reported here. The higher value,  $180 \text{ J/mm}^3$ , is beyond the limit between the steady region and the balling/keyhole region.

The process parameter ranges considered for the generation of the different conditions (called ‘treatments’ in Table 2) were large compared with previous works [16, 17] because the objective is to study the influence of a large variation of process parameters. In this work, the range considered for the individual parameters is  $\pm 50\text{--}100\%$ :

- Exposure time  $m$ ,  $75 \leq t \leq 280 \mu\text{s}$ .
- Point distance  $35 \leq d_p \leq 85 \mu\text{m}$ .
- Hatch distance  $75 \leq d_h \leq 124 \mu\text{m}$ .

Power was varied at two values only: 150 W and 200 W. Power values lower than 150 W did not ensure full powder melting even when varying all the other parameters. On the other hand, 200 W is the maximum power available in the industrial system.

Two samples were produced for each treatment. The experimental design could not be a standard  $2^k$  factorial design because of the constraint on the energy density value. The treatments in Table 2 do not result in the exact value of energy density, but a slight variation of  $\pm 2 \text{ J/mm}^3$  was deemed acceptable.

The meander scanning strategy was applied to all samples. In this configuration, the laser moves in a straight line vector from each side of the border. The scanning lines’ direction is

rotated by  $67^\circ$  at each layer. Hatch lines were scanned first, followed by two contour lines. All samples were built in the vertical position ( $90^\circ$ ) and no preheating was applied.

### 2.3 Mechanical properties

Samples were characterised in terms of apparent density, cross sections and tensile properties. Archimedes’ method was used to evaluate the apparent density of each sample. An electronic scale with a kit for density measurement was used (Sartorius YDK 01). The apparent density  $\rho_A$  was evaluated according to the following formula:

$$\rho_A = \frac{W_a \cdot \rho_{fl}}{W_a - W_{fl}} [\text{g/cm}^3],$$

where  $W_a$  [g] is the weight of the specimen in the air,  $W_{fl}$  [g] is the weight of the specimen in water and  $\rho_{fl}$  [ $\text{g/cm}^3$ ] is the density of the water. Measurements both in water and air were repeated three times. A suitable measurement method should be identified to analyse the porosity structure. There are typically three methods to measure part porosity content: Archimedes method, metallurgical sections and XCT [28]. Archimedes method is considered reliable and accurate but provides only a macroscopic result, as specific information on the position, shape and size of pores cannot be derived. On the contrary, metallurgical sections can provide location and size information on pores but only on predefined planes, and a large amount of cross-sectional analysis is required to obtain statistically representative data on part density. Moreover, the pores detected in 2D images can provide only a general indication of the size and shape of the actual 3-dimensional volume, as shown in Fig. 3. While a spherical pore can be easily observed in different cross-sections resulting in several circular shaped 2D voids (see Fig. 3a), a single lack of fusion pore might appear as a set of small pores in different sections (see Fig. 3b). Therefore, detecting irregular pores with metallurgical sections might generate large variability and less accuracy than Archimedes method, as results strongly depend on the analysed sections. X Ray-CT allows full 3D information on the pores’ size, shape and position to be obtained, so that a complete characterisation of the porosity structure can be ascertained.

Tensile properties were computed according to standard ASTM E8/E8M-16a, considering a geometry of the tensile specimens shown in Fig. 4. The machine used for the tensile test was an MTS Alliance RF/150. Samples were tested in the ‘as-built’ condition, without any post-processing.

**Table 2** Chemical composition of AISI 316L powder in wt%

Powder material	Fe	C	O	Si	Ni	Mo
AISI 316L	Balance	0.019	0.022	0.67	13	2.36

**Fig. 3** D reconstruction of pores produced by the L-PBF process

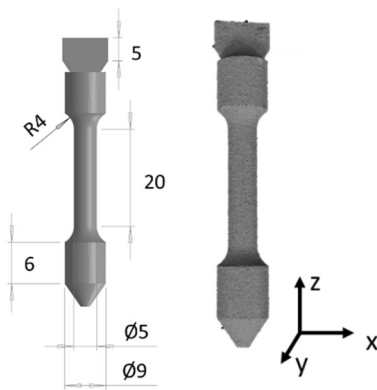
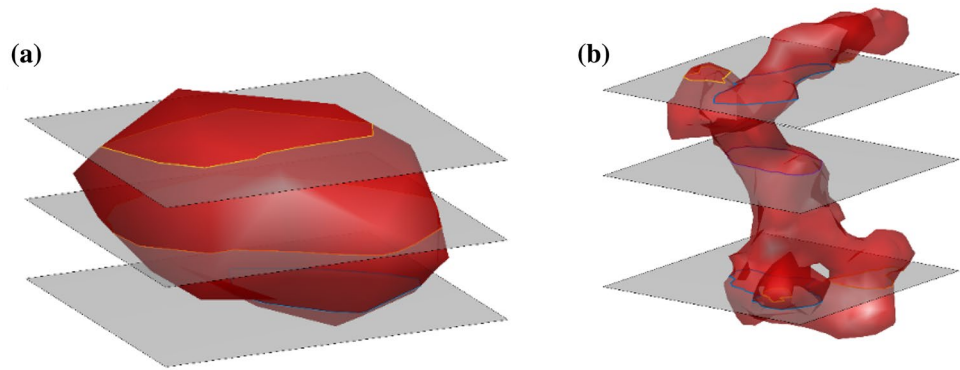


**Fig. 4** Tensile specimen dimension and coordinate system, dimensions are in mm

Samples were prepared by grinding and polishing, and V2A etching was used to perform the microstructural analysis.

## 2.4 XCT measurement

The tensile test samples were analysed by X-ray Computed Tomography. Scans were performed using a Nikon XT H 225 machine. Considering only the gauge length as the region of interest, samples were positioned close to the X-ray gun to obtain a high resolution, with a voxel size of  $14.8 \times 14.8 \times 14.8 \mu\text{m}^3$ . During all scans, the scanning parameters were kept constant. 10 W of power and an acceleration voltage of 150 kV were used. A 1.25 mm Cu filter was used throughout all the measurements to reduce the beam hardening effect. The scan parameters are reported in Tables 3, 4.

The power of the XCT was kept below 10 W, with a standard focus setting. Above this power, the auto-defocus setting was used to avoid damage to the detector. Each sample was positioned in the XCT using a fixture, which allowed us to obtain the XCT measurements of the same portion of the sample.

Reconstruction was performed using Nikon CTPro 3D, and surface determination was performed using VGStudio MAX 3.0. The local iterative surface determination algorithm was used to create the STL file with a search distance of 4 voxels. The region of interest (i.e., the part and the pores) was converted to mesh using the VGStudio MAX ‘Precise’ setting. The threshold was selected manually, and it is the starting point for the iterative surface reconstruction.

The surface was divided into the individual pores using Matlab and the geom3d package [29]. The procedure allows the properties of each pore to be measured, i.e., the volume  $V$ ; the position of the centroid described using a cylindrical coordinate system in which the radial position is indicated with  $\rho$ ; the surface area,  $A$  and the bounding box. The bounding box refers to the elongation of each sample along the  $X$ ,  $Y$  and  $Z$  planes (see Fig. 5) where  $\Delta X = X_{\max} - X_{\min}$ ,  $\Delta Y = Y_{\max} - Y_{\min}$ , and  $\Delta Z = Z_{\max} - Z_{\min}$  represent the elongation of each pore along the three different directions.

Eventually, the sphericity of the pore was evaluated as [30]:

$$\psi = \left( \frac{36 \cdot \pi \cdot V^2}{A^3} \right)^{1/3}$$

where  $V$  represents the pore volume and  $A$  the surface area. A sphericity index close to 1 means that the shape of a pore is similar to a sphere. As the sphericity index decreases, the shape of the pore becomes more irregular.

All pores with less than  $2^3$  voxels were considered ‘noise’ and eliminated from the analysis.

### 2.4.1 Porosity indexes

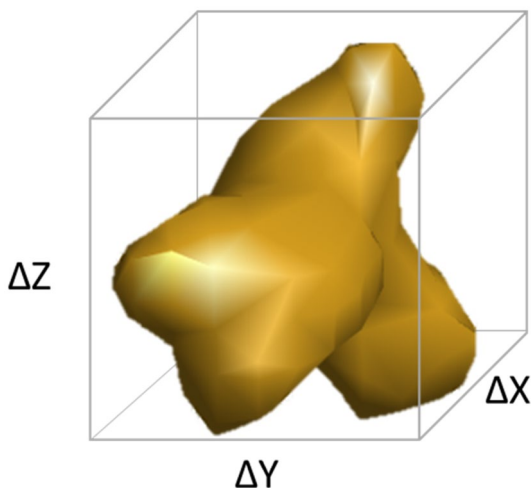
Several metrics have been proposed in the literature to characterise pore networks. The most commonly used are the pore with the maximum volume, total pore count, average equivalent pore diameter and maximum equivalent pore diameter [27]. For the present work, two indexes were used based on the information obtained in the literature. The objective was to identify

**Table 3** Process parameters used in the experimentation

Treatment	P [W]	t [ $\mu$ s]	dp [ $\mu$ m]	dh [ $\mu$ m]	$E_d$ [J/mm <sup>3</sup> ]	Samples ID
1	150	77	38	102	59.6	S1; S2
2	150	100	42	121	59.0	S3; S4
3	150	118	60	99	59.6	S5; S6
4	200	75	42	121	59.0	S7; S8
5	200	88	60	99	59.3	S9; S10
6	200	90	59	103	59.2	S11; S12
7	150	83	85	243	103.3	S13; S14
8	150	116	45	178	102.3	S15; S16
9	150	96	53	176	103.8	S17; S18
10	200	103	85	224	103.8	S19; S20
11	200	76	76	148	102.5	S21; S22
12	200	121	44	137	102.9	S23; S24
13	150	277	44	106	178.2	S25; S26
14	150	230	42	91	180.5	S27; S28
15	150	161	35	76	181.6	S29; S30
16	200	229	68	75	179.6	S31; S32
17	200	146	35	93	179.4	S33; S34
18	200	205	48	95	179.8	S35; S36

**Table 4** XCT scanning parameters

Parameter	Value
Filter material	Copper
Filter thickness	1.25 mm
Acceleration voltage	150 kV
Exposure time	2000 ms
Voxel size	14.8 $\times$ 14.8 $\times$ 14.8 $\mu$ m <sup>3</sup>
Number of images per projection	2

**Fig. 5** Example of Bounding Box

two indexes that could consider the amount of porosity and the distribution of the pore location within a sample. These two aspects (volume and position) are considered the most important features affecting the mechanical properties [26, 31], and [32]. Chawla and Deng [31] investigated the effect of the pore structure on porous sintered steel materials, and they found that pore clustering acts as stress concentration, reducing the tensile and fatigue properties of the parts. Biswal et al. [32] investigated the effect of the pore structure on the fatigue properties of additively manufactured Ti6Al4V alloy. Their results showed that a critical aspect is the location of the pores: pores close to the surface significantly decrease the mechanical performance. The results obtained by Zhang et al. [26] were discussed in the introduction. In conclusion, two indexes of porosity are considered in this paper to study the influence of the pores' volume and position on the mechanical properties of the parts:

Maximum Volume Reduction along the building direction,  $\Pi$ , an index proposed by [26] for high-pressure die casting processes. The index is computed by dividing the scanning region of each sample in a set of layers, considering the Z-axis (i.e., the building direction) as reference. In our case, a set of 150 layers was considered with a height of 0.05 mm each, which corresponds to the layer thickness of the L-PBF process. In other words, the first layer is the one between 0 mm and 0.05 mm, the second layer is constrained by 0.051 and 0.100 mm and so on. The pores with the centroid belonging to each layer are then extracted and their volumes summed up. For each sample  $j$ , the worst layer (i.e., the layer with the highest porosity) is then selected as well as the corresponding value of total pore volume indicated with  $\Pi_j$ .  $\Pi_j$  combines the effects of pore volume and

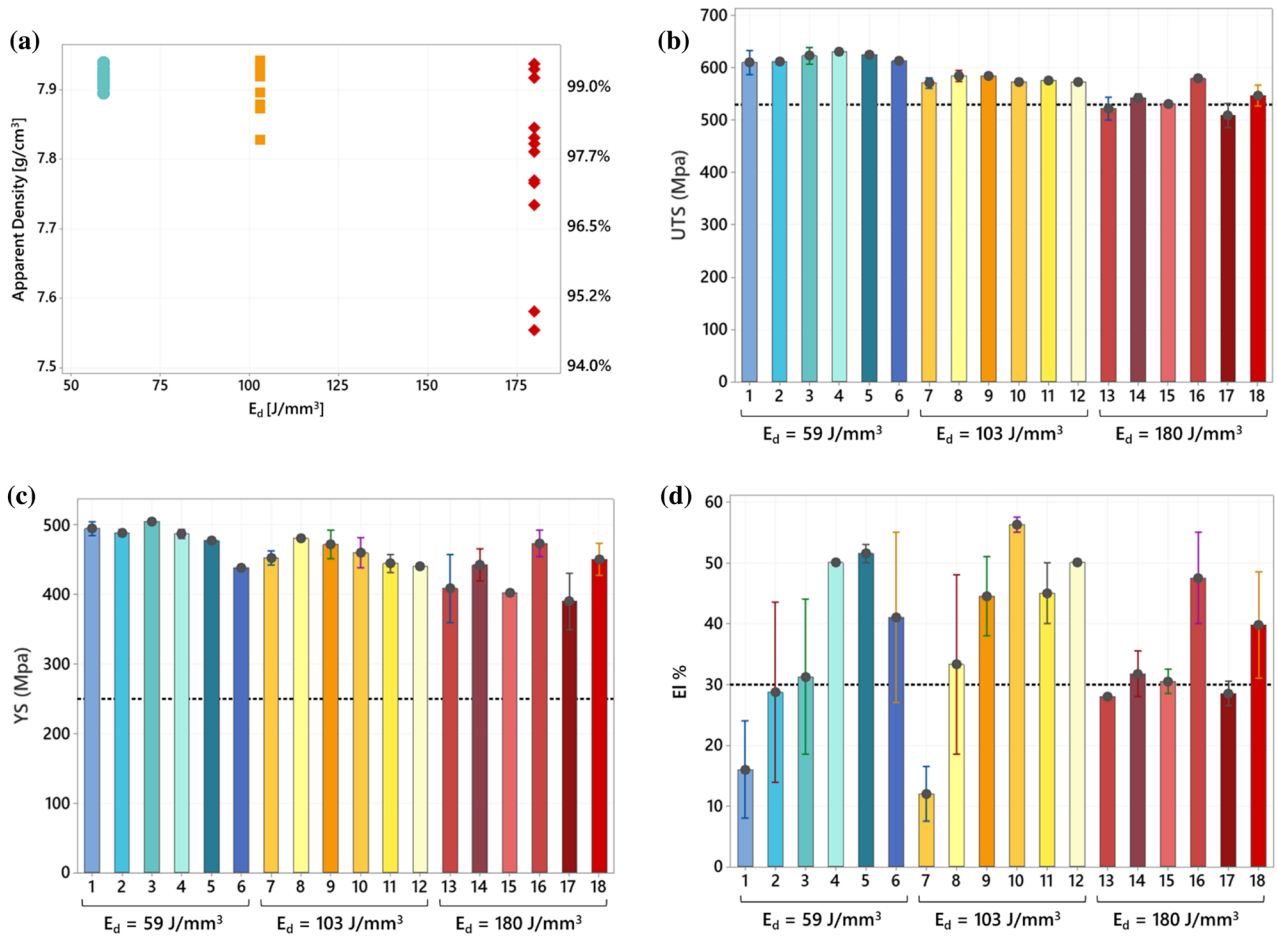


**Fig. 6** Mechanical properties of 316L samples during the different treatments (Table 2) **b** UTS, **c** Yield strength, **d** Elongation El %. Bars represent  $\pm 1$  standard deviation

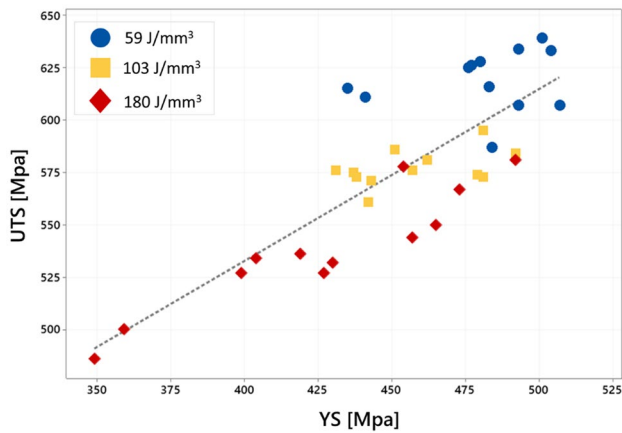


**Fig. 7** Correlation between UTS and YS

spatial correlation as high values of  $\Pi_j$  indicate the presence of pores concentrated in a small region of the sample.

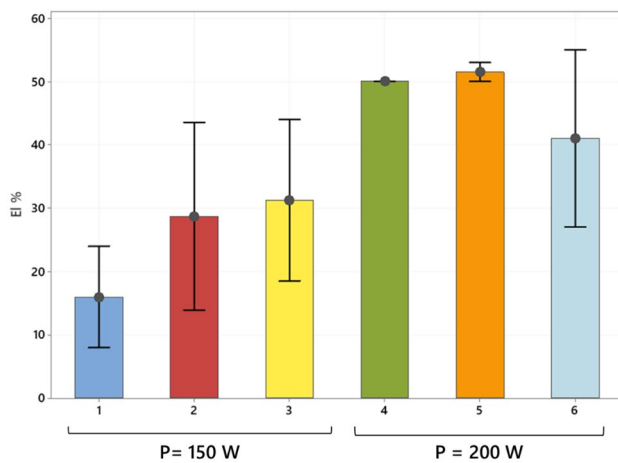
Radial Equivalent Distance, RED. The radial equivalent distance is an index that weighs the pores' volume based on their distance from the centre of the sample in the XY plane. This index is based on the concept that the most critical pores are large pores near the edge of the sample; the less critical ones are small pores near the centre [32]. The RED index is based on the porosity index defined in [27], where it was found to correlate with the tensile properties. More specifically, the RED index is given by:

$$RED_j = \frac{1}{V_{tot}} \sum_{i=1}^{N_j} V_i e^{\frac{-|g-\rho_i-r_{eq,i}|}{g\gamma}} \quad (2)$$

where  $V_{tot}$  is the total volume of the gauge length,  $N_j$  is the number of pores in the  $j$ -th sample,  $g$  is the nominal radius of the sample in the gauge,  $\rho_i$  is the radial position of the  $i$ -th pore in the XY plane,  $r_{eq,i}$  is the equivalent radius of the  $i$ -th pore and  $\gamma$  is a smoothing parameter. The weight function selected is exponential with smoothing parameter  $\gamma$ . A small

**Table 5** Mechanical properties of 316L processed with L-PBF

	Energy density [J/mm <sup>3</sup> ]	Power [W]	UTS [MPa]	YS [MPa]	EL %
Present work	59	150	623 ± 6.59	467 ± 23	47.5 ± 10
		200	614 ± 19.0	495 ± 10	25.3 ± 15
	103	150	580 ± 11.6	468 ± 19.3	29.9 ± 18
		200	574 ± 2.0	448 ± 18.5	50.4 ± 6
	180	150	532 ± 17.5	417 ± 39.4	30.1 ± 3
		200	545 ± 37.0	438 ± 50	38.6 ± 11
[33]	48	180	524	385	22
[34]	20	90	509.0 ± 3	430.4 ± 11	12.4 ± 1
[35]	81	100	687 ± 40	517 ± 38	32 ± 5
ASTM F3184-16 'stress relieved'			515	205	30

**Fig. 8** Elongation values at treatment level for E<sub>d</sub> = 59 J/mm<sup>3</sup>. Bars represent ± 1 standard deviation

value of  $\gamma$  results in less weight imposed on the pores far away from the centre, a larger value of  $\gamma$  results in a slower decay of the weight function, therefore reducing the effect of the distance of the pores on the value of the index. In our case,  $\gamma$  was set equal to 0.2 [27].

### 3 Tensile tests results and discussion

In this section, the results of the tensile tests along with the fractographic analysis are discussed. A regression model is finally proposed to predict UTS based on the VED.

#### 3.1 Static mechanical properties

The results of the mechanical properties of the samples are listed in the Appendix. The density of all samples is higher

**Table 6** Reference samples used for SEM analysis

Treatment	Power	Elongation	Name
3	150	44	S5
3	150	19	S6
6	200	55	S11
6	200	27	S12

than 94% (considering 7.98 g/cm<sup>3</sup> as the reference value). The apparent density changes with the VED as expected. The scatterplot in Fig. 6a also shows that as the VED increases, the variability of the apparent density increases as well and high-density samples can sometimes also be obtained with large values of VED. Similar results were obtained in [33]. The two samples at 180 J/mm<sup>3</sup> resulting in low apparent density were produced with different settings of process parameters, therefore their low performances cannot be ascribed to the processing conditions but to the inevitable variability of the process.

The range of energy density between 59 and 103 J/mm<sup>3</sup> belongs to the steady region as identified in Fig. 1,

while at 180 J/mm<sup>3</sup>, the apparent density is lower, indicating keyhole and balling phenomena. Tensile test results are illustrated in Fig. 6b–d. UTS and YS show a linear reduction in energy density, as expected based on the apparent density data. Dotted horizontal lines were added in correspondence to the reference values of AISI 316L processed via L-PBF according to standard ASTM F3184-16 (UTS = 530 MPa, YS = 240 MPa, and EI = 30% for the annealed condition). UTS and YS are also highly correlated in the range of energy density considered, as shown in

Figure 7, showing a Pearson's correlation coefficient equal to 0.808 (with a 95% confidence interval of [0.652;0.898]).

The variability observed on the elongation is much larger than the one observed on UTS and YS and appears to be more



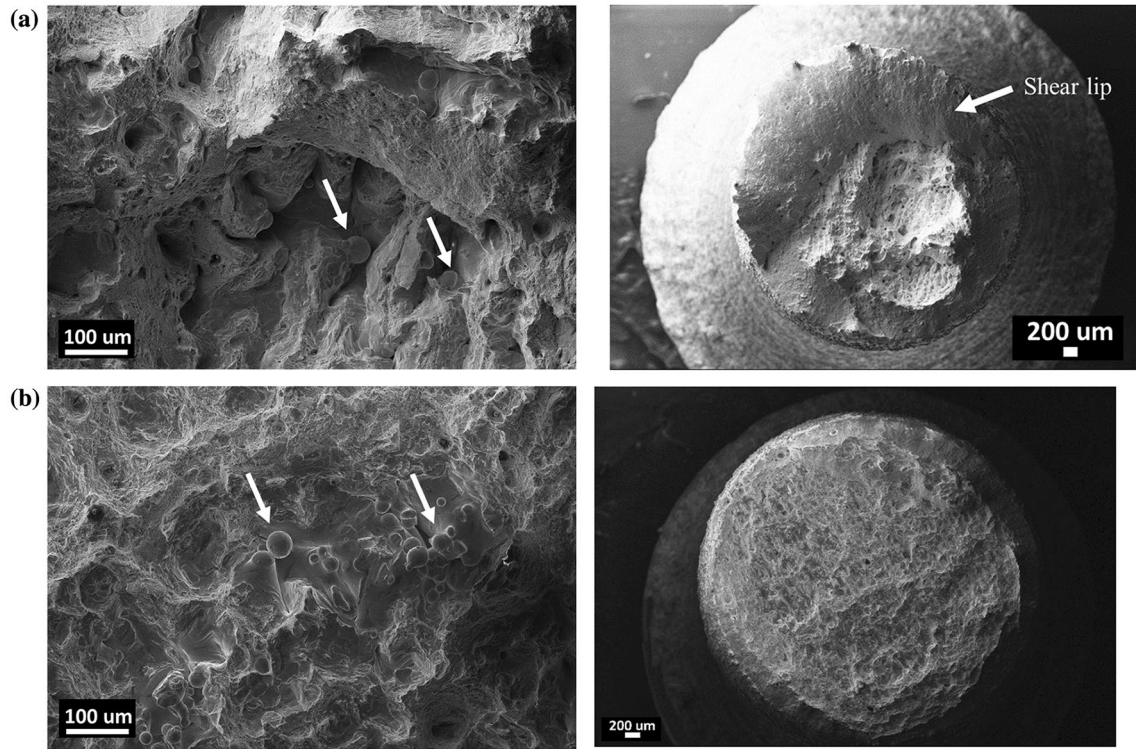


Fig. 9 SEM images of the fracture surface of replicated samples produced using treatment 3 and P=150 W a Sample S5, b Sample S6

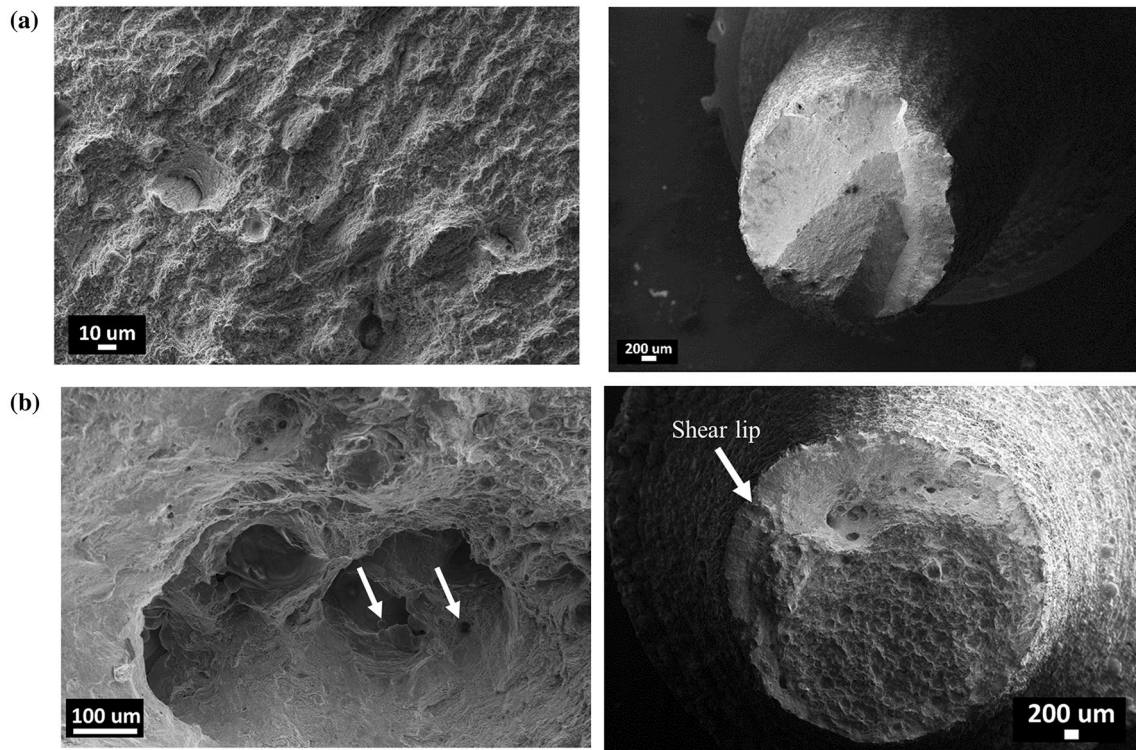
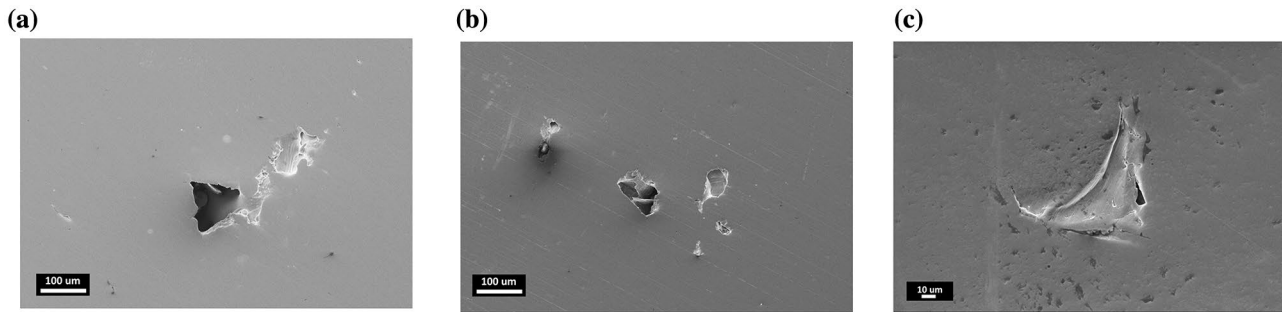


Fig. 10 SEM images of the fracture surfaces of replicate samples using treatment 6 and P=200 W a Sample S11, b Sample S12



**Fig. 11** SEM cross-sectional images for reference samples. **a** Treatment 3, elongation 44% (Sample S5), **b** treatment 3 (Sample S6) elongation 18.5% and **c** treatment 6, elongation 27% (Sample S12)

severe when the optimal VED ( $59 \text{ J/mm}^3$ ) is assumed. Moreover, the elongation seems to be driven by other factors than process parameters and VED as different values of elongation can be observed both on different treatments at the same VED and on different replicates during the same treatment.

Table 5 shows a synthetic summary of mechanical properties observed in our study along with the ones reported in the literature.

In summary, the macroscopic characterisation of our experimental study showed that:

- UTS and YS decrease as the VED increases. Despite the reduction in UTS and YS, the resulting properties are coherent with the reference values for the material. In general, it appears that even a considerable variation of process parameters (and VED) does not cause a considerable variation in UTS and YS. UTS and YS are highly correlated in the process window considered.
- Elongation varies significantly among the treatments and among replicates in the treatments.

Based on these results, a linear model can be fitted to describe UTS as a function of the energy density VED (note that YS cannot be included as a regressor, as it is highly correlated with UTS).

The estimated model  $\widehat{UTS}(VED)$  is given by:

$$\widehat{UTS} = 574.64 - 39.13 \cdot VED (\text{adj-}R^2 = 73.04\%).$$

The regression equation indicates a statistically significant decrease in UTS as energy density VED increases; this result is expected because of the considerable variation of energy density and process parameters considered in the experiment. Nevertheless, all the samples sharing the same energy density value show similar UTS values (as visible in Fig. 6b). This finding was unexpected because the large variation of individual process parameters was supposed to influence UTS (and YS); the result shows that using the same energy density does not influence UTS and YS even when a large variability of process parameters is considered.

On the contrary, it is not possible to derive a relationship between the elongation and the energy density, and therefore a different approach should be considered. The analysis of the elongation data will focus on the samples produced at the lowest energy density value only. In fact, this value belongs to the steady region of the parameters (apparent density  $> 99\%$ ) and low-energy density results in high build rates, too. Therefore, these parameters are the most likely to be used in all industrial environments.

First, a fractographic analysis is performed to investigate the different fracture surfaces obtained in the tests, and later, a more detailed analysis of the XCT data is carried out. The objective is to find an equation to predict the elongation values with the porosity indexes defined in Sect. 2.4.1.

### 3.2 Fractographic analysis

The fractographic analysis focuses on samples produced at energy density level  $59 \text{ J/mm}^3$ . The detailed elongation results at  $59 \text{ J/mm}^3$  are illustrated in Fig. 8, where elongation data are visualised for each treatment level (1–6, as stated in Table 3).

Samples produced at  $P=150 \text{ W}$  are characterised by a lower elongation than samples at  $P=200 \text{ W}$ . Furthermore, sample S12 (treatment 6) printed at  $P=200 \text{ W}$  presents a low elongation value, while its replicate (sample S11) shows standard properties.

The effect of changing power at a fixed energy density on tensile properties of L-PBF parts was already investigated in the literature [24]. Using AlSi10Mg powder, the authors found that the power influences the UTS, while also showing a limited effect on the elongation. However, results obtained in [24] for aluminum alloy cannot be transferred to our case as the material used in our study is different.

An interesting result observed in our experiments is the variability of elongation values observed on specimens produced with the same parameters (same treatment). To better study this variance, SEM images of fracture surfaces and cross sections on four reference samples were analysed. The reference samples are selected as replicated conditions

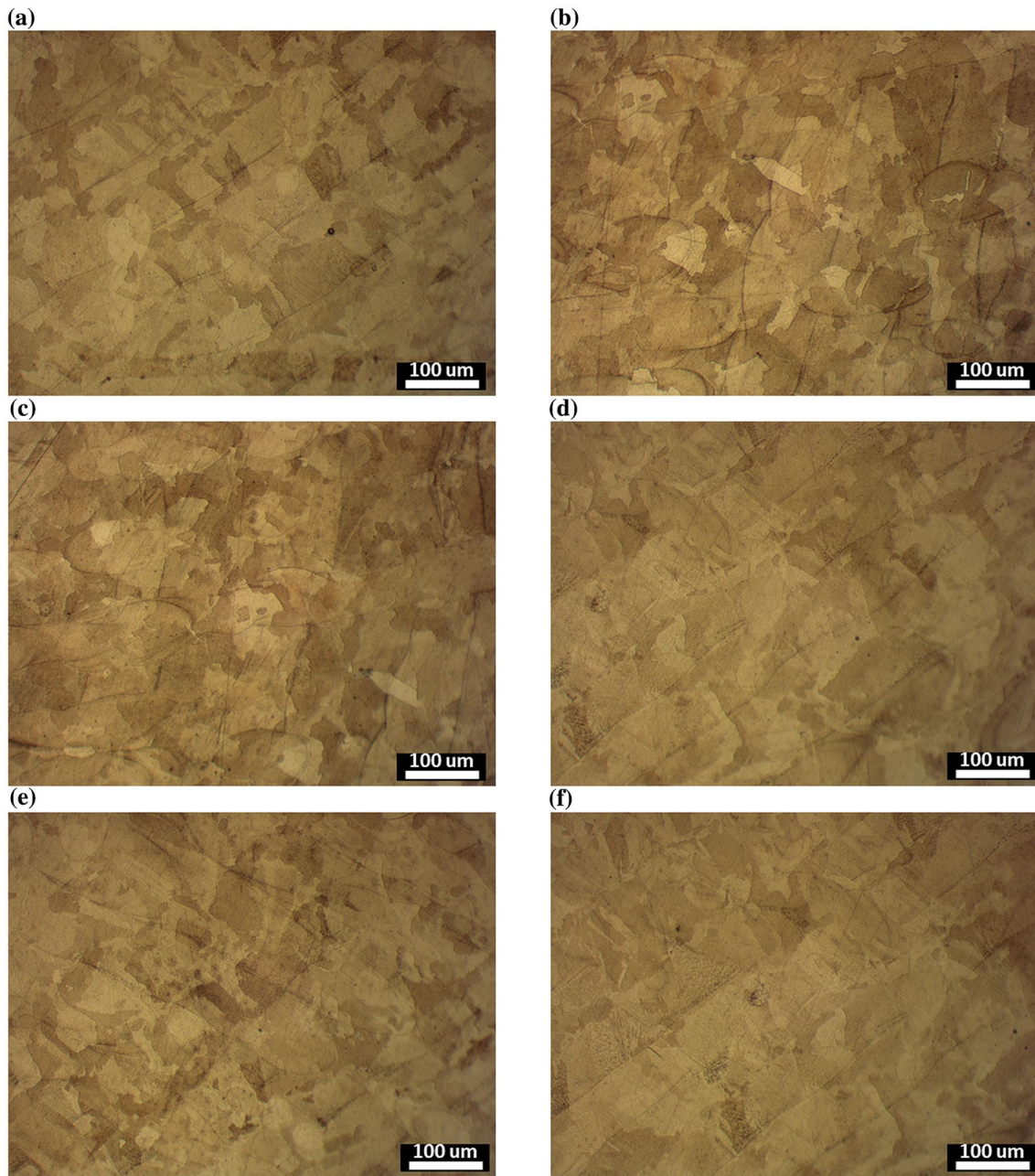


**Fig. 12** Cross-sectional views on the XY plane of samples at different treatments **a** treatment 1, **b** treatment 2, **c** treatment 3, **d** treatment 4, **e** treatment 5 and **f** treatment 6

of two treatments, namely treatments 3 and 6; in these two conditions, the replicated samples show a large variability of elongation values.

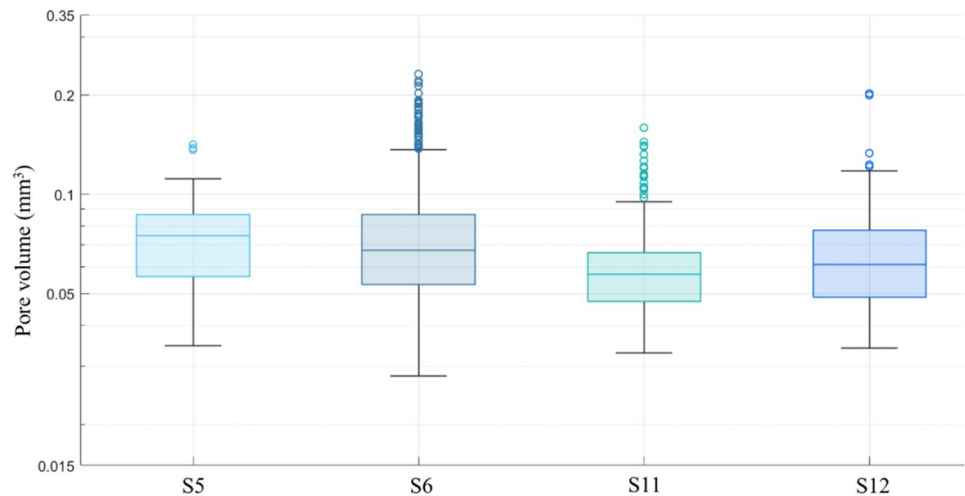
The samples considered for the SEM analysis are reported in Table 6.

In Fig. 9, the SEM fracture surfaces of two samples produced using treatment 3 are illustrated. Sample S5 in Fig. 9a obtained an elongation of 44%, while sample S6 in Fig. 9b resulted in low elongation (18.5%). In the first sample, the

fracture surface shows unmelted particles, especially at the centre of the surface. In addition, the upper edge contains a pronounced shear lip. In the latter case, several unmelted particles are visible on the surface, which explains the low elongation. The fracture surface is homogeneous, and the shear lip is not visibly different from the previous case.

In Fig. 10, fracture surfaces of samples produced using treatment 6 are shown. Sample S11 in Fig. 10a obtained an elongation of 55%. The fracture surface has a homogenous

**Fig. 13** Volume distribution for the reference samples. Volume data were transformed with a natural log transformation



structure and no visible defects are detected. The dimples are visible only at high magnification. Sample S12 in Fig. 10b is characterised by a low elongation (27%). The fracture surface is entirely different from its replicate in Fig. 10a. Dimples are visible at lower magnification, and the shear lip is present in the upper part of the specimens as it was for the sample in Fig. 9a. Cavities and minor porosity are found on the surface.

Samples were cross-sectioned and polished to obtain SEM images of defects. The porosity found for the reference samples is shown in Fig. 11. Samples S5 and S6 are characterised by large and irregular porosity, probably due to a lack of fusion. The detected defects have a size of around 100  $\mu\text{m}$  and are scattered along the entire surface. In samples S11 and S12, a few defects are found, mainly with a regular shape. However, irregular pores are also detected for sample S12. Compared with the low-power samples, the irregular pores found at  $P=200$  W have a smaller size (around 50  $\mu\text{m}$ ).

Generally, pores detected for  $P=150$  W are large and irregular, while at  $P=200$  W, spherical pores are mostly found. The irregular porosity at  $P=200$  W has a smaller size than the ones at  $P=150$  W. A deeper analysis of the pore structure is required to understand the effect of the pore structure on the elongation of the samples.

The microstructure on the XY plane of reference samples during the different treatments was analysed using an optical microscope. The optical micrographs illustrated in Fig. 12 show identical features for all samples produced at 59  $\text{J}/\text{mm}^3$ ; the laser scans are visible with well-defined melt pool boundaries. The microstructure does not vary despite changing the process parameters using the same volumetric energy density.

In conclusion, the investigation of the cross-sections and the fracture surfaces of selected specimens did not help

identify a possible explanation for the considerable variation in elongation.

## 4 XCT analysis

For the qualitative XCT analysis, the focus is on the reference samples in Table 6. Then, a correlation between elongation and the porosity indexes for all samples produced at 59  $\text{J}/\text{mm}^3$  is carried out.

### 4.1 Porosity structures

This section focuses on the porosity structure of the samples produced with the combination of parameters that resulted in different elongation values. The objective is to understand what difference in porosity structure between these samples caused the premature failure.

Box plots showing the logarithmic transformation of the volume distribution are shown in Fig. 13. The median values of the volume distribution do not vary among the considered samples. Samples S6 and S11 are characterised by a skewed distribution with an increased presence of larger pores. The low limit for all volume distribution is similar because data are cut off, as explained in Sect. 2.3. The volumes' distributions do not differ significantly, as expected from the mean density measurements performed using Archimedes method.

In all four cases, the pores are elongated along the XY direction rather than on the Z direction, as shown by the histograms in Fig. 14. This result is coherent with the literature [38] and [23]. Samples S6 and S12 present the largest values of  $\Delta X$ ,  $\Delta Y$  and  $\Delta Z$  compared with their respective replicates. Smaller pores characterise the samples produced at  $P=200$  W (Treatment 6) in all directions.

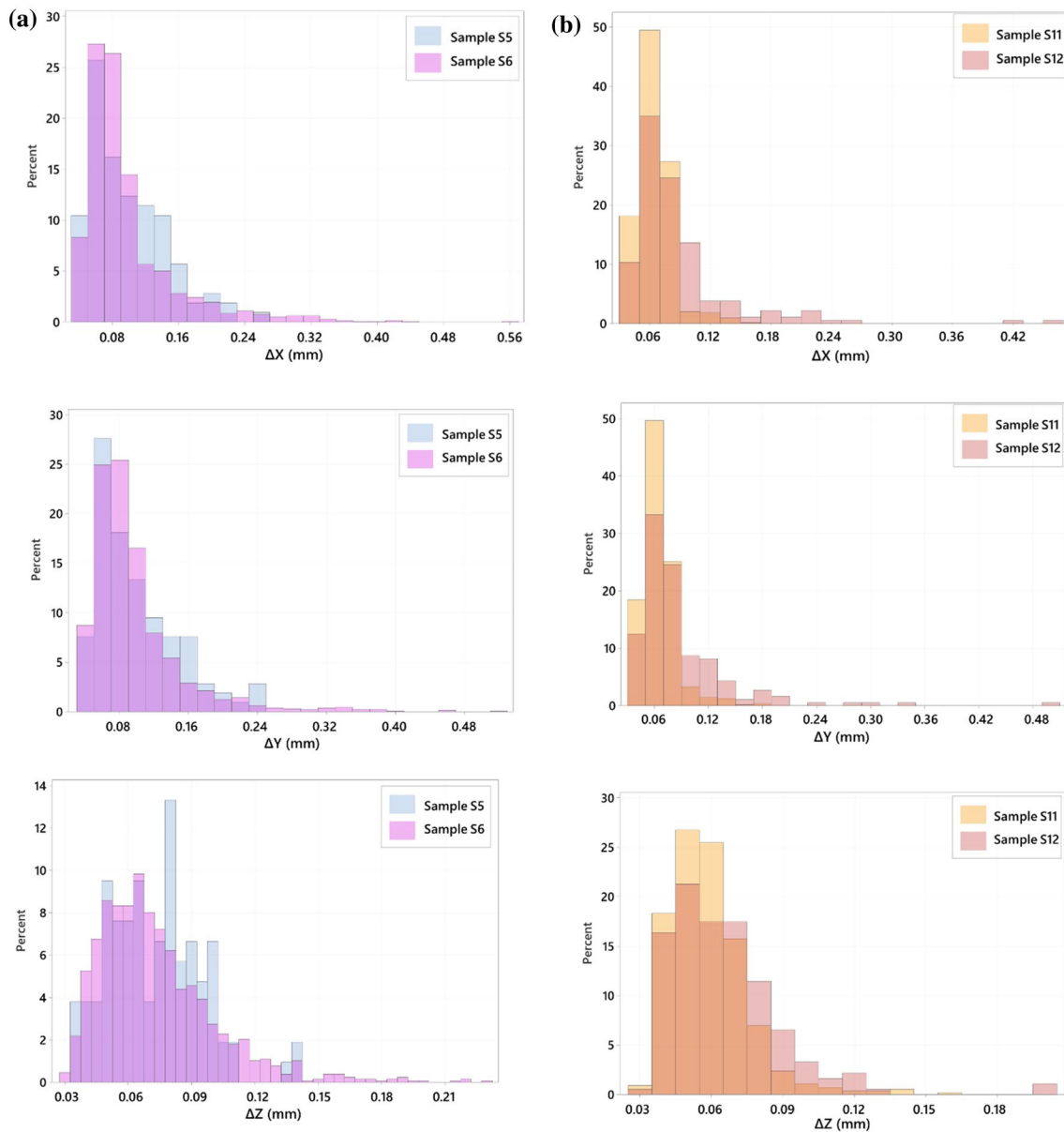


**Fig. 14** Elongation of the pores along the X-, Y- and Z-axis. **a** Samples S5 and S6, **b** samples S11 and S12

The relationship between the pores' size and shape is shown in Fig. 15, where each dot represents a pore. The shape distributions of the pores do not change among the different samples in Fig. 15 so it cannot explain elongation differences, as suggested in the literature [25]. Interestingly, high spherical pores are also found for large pores ( $\Delta Z$  between 0.08 and 0.10 mm), independent of the power used. In addition, irregular pores are also found in samples S11 and S12 (Fig. 15b), indicating that occasionally a lack of fusion defects can be generated even when optimal energy density and high power are used. Samples S5 and S6 in Fig. 15a are characterised by a more irregular shape of the pores as the minimum value of the sphericity index is close

to 0.3. The presence of highly irregular pores is expected at low-power values.

The position of the pores inside the sample is also investigated. The histograms shown in Fig. 16 represent the distribution of pore position along the radial direction. Pores are mainly positioned near the sample edge, 500–200  $\mu\text{m}$  from the edge. These pores are usually formed at the interface between the end of the melt track and the contour lines [11]. The distribution of pore location is similar in all the considered samples.

From this qualitative analysis, it can be concluded that:

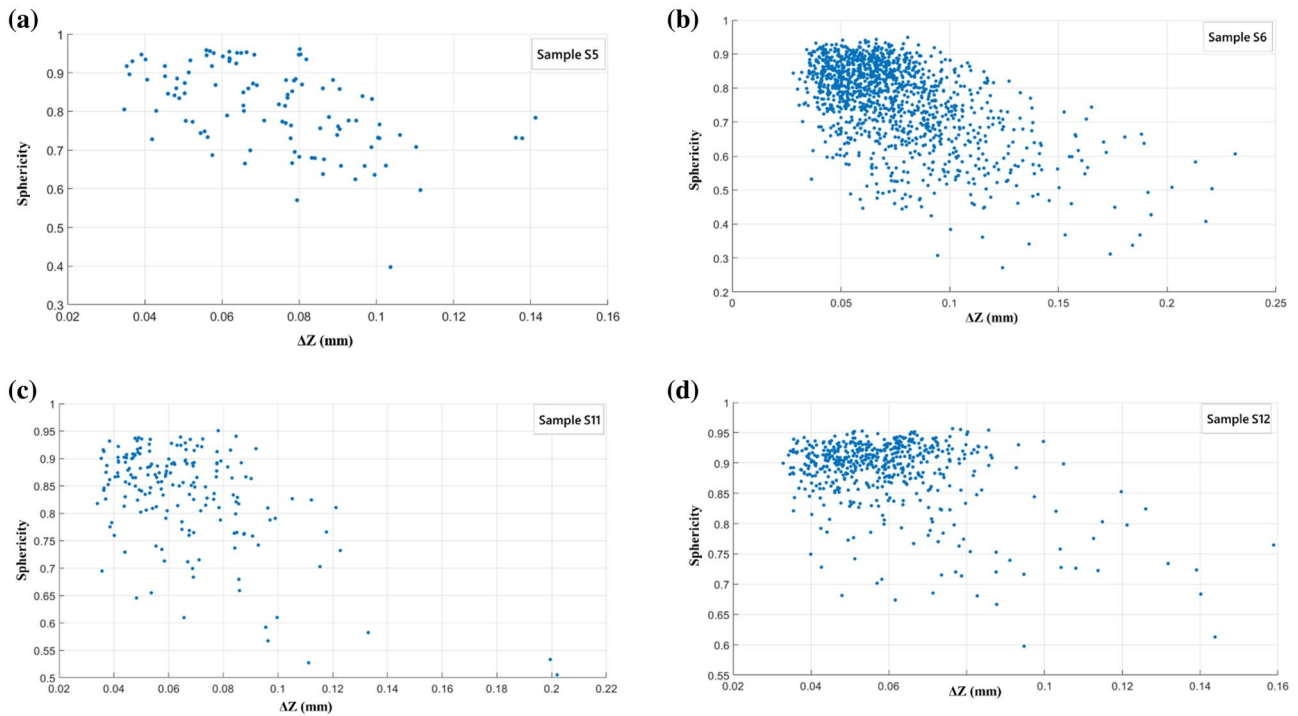


**Fig. 15** Relationship between the pores' size ( $\Delta Z$ ) and sphericity for the four samples **a** Sample S5, **b** sample S6, **c** sample S11 and **d** sample S12

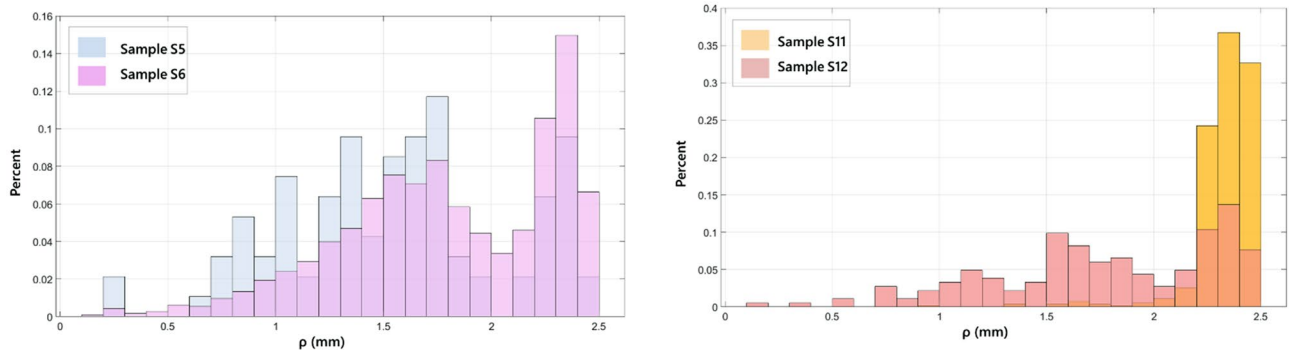


**Fig. 16** Distribution of the pores along the radial position  $\rho$

Pores are more elongated along the XY plane than the Z plane for all samples. This result was also found in [21, 23, 38].

The morphology of the pores is similar for all samples.

The position of the pores is similar for all samples, with a peak of porosity at the hatch-contour interface.

The qualitative analysis shows that the porosity structure is different among the samples even if the apparent density is similar; this result is coherent with Kim et al. [23]. The samples with the lowest elongation show the largest pores.

### 4.2 Relationship between porosity structure and elongation

The relationship between elongation and the porosity index defined in Sect. 2.4.1 is presented in Fig. 17.

The trend between elongation and  $\Pi$  is clear for energy density  $59 \text{ J/mm}^3$ : a substantial decrease in elongation as the cross-sectional area is reduced. The same index was used in [26] for the high-pressure die casting process, and a statistical correlation between porosity and elongation was found.

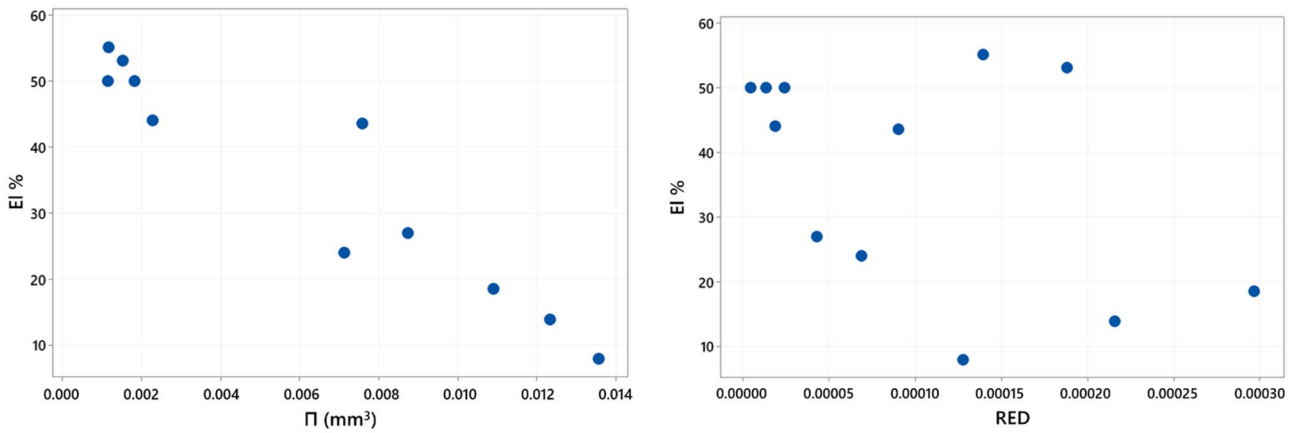


Fig. 17 Correlation between **a** elongation and volume-based index  $\Pi$  **b** elongation and position-based index RED

**Table 7** Regression equations for elongation as a function of porosity index  $\Pi$  at a fixed energy density,  $VED = 59 \text{ J/mm}^3$

Regression equation	adj- $R^2$	$MS_E$
$\hat{E}l_{\%} = 31.09 - 20.9\Pi$	90.19%	28.18

the position of the pores (RED index) does not influence the mechanical properties.

It is possible to estimate a regression equation in the form  $\hat{E}l_{\%} = \hat{E}l_{\%}(\Pi | VED = 59 \text{ J/mm}^3)$ . The equation is given in Table 7 and it is shown Fig. 18.

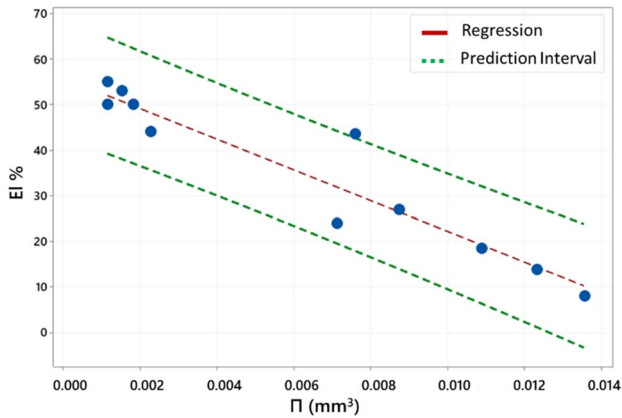


Fig. 18 Relationship between the highest volume reduction ( $\Pi$ ) and elongation. Dotted lines represent the prediction interval

The position-based index (RED) proposed in the literature [27] for L-PBF processes does not show any correlation with the elongation. At  $E_d = 59 \text{ J/mm}^3$ , similar values of RED result in an extensive range of elongation, indicating a low correlation between pore position and elongation: the correlation coefficient is 0.460 (95% confidence interval for the correlation coefficient is  $[-0.818; -0.154]$ ).

In conclusion, the elongation is highly correlated with a volume-based index rather than a position-based index. The clustering of pores is detrimental to the mechanical properties, especially elongation, while UTS and YS were not affected by the porosity structure. Based on the result of the analysis,

## 5 Conclusion

This work investigates the influence of a wide variation of process parameters on the tensile properties of AISI 316L processed via L-PBF. Three levels of energy density were selected, ranging from the optimal region ( $59 \text{ J/mm}^3$ ) to the keyhole region ( $180 \text{ J/mm}^3$ ), and each level was obtained using different combinations of individual process parameters, namely power, point distance, hatch distance and exposure time.

Specimens were analysed in terms of the average apparent density, XCT scan and tensile properties. The results showed that the UTS and YS varied according to energy density: as the energy density decreases towards non-optimal values, UTS and YS reduce. Interestingly, even with a significant variation of process parameters, energy density is still a good predictor for tensile strength (adj- $R^2 = 73\%$ ), while UTS and YS are shown to be highly correlated.

Elongation was found to vary quite significantly even considering samples produced at the same energy density, which contrasts with the results of UTS and YS. By considering only the optimal level of energy density, XCT data were used to find a statistical correlation between specific features of the observed porosity and the final value of elongation observed, as suggested by the literature. Two indexes were proposed to characterise the distribution of the pores: a layer-wise volume-based index ( $\Pi$ ) and a position-based index (RED).  $\Pi$  index was able to predict the sample elongation with a very good statistical

fit ( $\text{adj-R}^2=91\%$ ), while the RED index did not show a good correlation with elongation. In conclusion, the clustering of the pores influences the elongation rather than the position of the pores inside the sample.

Further studies will focus on extending the experimental investigation to consolidate our results and better investigate the effect of process parameters. Additional models will also be investigated to increase the prediction ability of porosity

indicators in terms of final mechanical performances, particularly for fatigue properties.

## Appendix

See the below Table 8.

**Table 8** Complete list of experimental results

Treatment	P [W]	t [ $\mu\text{s}$ ]	dp [ $\mu\text{m}$ ]	dh [ $\mu\text{m}$ ]	UTS (Mpa)	YS (Mpa)	El%	Apparent density (g/cm <sup>3</sup> )	Ed [J/mm <sup>3</sup> ]	ID sample	$\Pi$ (mm <sup>3</sup> )	RED (-)
1	150	77	38	102	633	504	24	7.895	59	S1	0.007123	1.87E-05
1	150	77	38	102	587	484	8	7.894	59	S2	0.013556	2.43E-05
2	150	100	42	121	616	483	43,5	7.922	59	S3	0.007588	3.59E-04
2	150	100	42	121	607	493	13,9	7.910	59	S4	0.012325	9.34E-05
3	150	118	60	99	639	501	44	7.915	59	S5	0.002282	9.01E-05
3	150	118	60	99	607	507	18,5	7.904	59	S6	0.010888	2.97E-04
4	200	75	42	121	628	480	50	7.929	59	S7	0.001822	1.79E-03
4	200	75	42	121	634	493	50	7.925	59	S8	0.001153	3.81E-03
5	200	88	60	99	626	477	53	7.939	59	S9	0.001526	2.19E-05
5	200	88	60	99	625	476	50	7.928	59	S10	0.001152	1.33E-05
6	200	90	59	103	611	441	55	7.937	59	S11	0.001163	3.10E-05
6	200	90	59	103	615	435	27	7.937	59	S12	0.008737	1.61E-04
7	150	243	85	83	581	462	7,5	7.925	103	S13	0.004104	7.98E-03
7	150	243	85	83	561	442	16,5	7.872	103	S14	0.019812	2.87E-03
8	150	178	45	116	595	481	48	7.919	103	S15	0.006657	3.41E-03
8	150	178	45	116	574	479	18,5	7.827	103	S16	0.069213	5.69E-04
9	150	176	53	96	584	492	51	7.922	103	S17	0.003051	1.54E-03
9	150	176	53	96	586	451	38	7.918	103	S18	0.038718	1.39E-04
10	200	224	85	103	573	438	57,5	7.921	103	S19	0.00505	1.54E-03
10	200	224	85	103	573	481	55	7.940	103	S20	0.001564	6.29E-04
11	200	148	76	76	576	457	50	7.942	103	S21	0.004279	2.29E-03
11	200	148	76	76	576	431	40	7.933	103	S22	0.005772	4.29E-05
12	200	137	44	121	575	437	50	7.878	103	S23	0.017251	6.87E-05
12	200	137	44	121	571	443	50	7.895	103	S24	0.017274	2.16E-04
13	150	277	44	106	544	457	28,5	7.831	180	S25	0.047352	1.88E-04
13	150	277	44	106	500	359	27,5	7.581	180	S26	0.083049	5.60E-03
14	150	230	42	91	550	465	28	7.845	180	S27	0.082203	1.28E-04
14	150	230	42	91	536	419	35,5	7.766	180	S28	0.034862	3.91E-03
15	150	161	35	76	527	399	32,5	7.734	180	S29	0.024098	4.37E-06
15	150	161	35	76	534	404	28,5	7.770	180	S30	0.033807	8.18E-05
16	200	229	68	75	581	492	55	7.937	180	S31	0.002338	3.76E-04
16	200	229	68	75	578	454	40	7.929	180	S32	0.003917	9.43E-03
17	200	146	35	93	486	349	30,5	7.553	180	S33	0.046878	7.32E-04
17	200	146	35	93	532	430	26,5	7.822	180	S34	0.038957	2.83E-03
18	200	205	48	95	567	473	48,5	7.917	180	S35	0.007024	2.25E-04
18	200	205	48	95	527	427	31	7.811	180	S36	0.033671	9.95E-05



**Acknowledgements** The present research was partially supported by the S.I.ADD Project (Soluzioni Innovative per la qualità e la sostenibilità dei processi di ADDitive manufacturing) “MIUR ARS01\_00806”. The Italian Ministry of Education, University and Research is acknowledged for the support provided through the Project ‘Department of Excellence LIS4.0 – Lightweight and Smart Structures for Industry 4.0’.

**Author contributions** SC: Conceptualization, methodology, software, investigation, Writing—Original Draft. LP: Methodology, software, data curation, Writing—Review & Editing. BMC: Conceptualization, Methodology, Supervision, Finding acquisition, Writing—Review & Editing. QS: Conceptualization, Methodology, Supervision, Finding acquisition, Writing—Review & Editing.

**Funding** The present research was partially supported by the S.I.ADD Project (Soluzioni Innovative per la qualità e la sostenibilità dei processi di ADDitive manufacturing) “MIUR ARS01\_00806”. The Italian Ministry of Education, University and Research is acknowledged for the support provided through the Project ‘Department of Excellence LIS4.0 – Lightweight and Smart Structures for Industry 4.0’.

**Availability of data and material** All relevant data are available in the manuscript.

## Declarations

**Conflict of interest** The authors declare no conflict of interest. The authors have no relevant financial or non-financial interests to disclose.

**Open Access** This article is licensed under a Creative Commons Attribution 4.0 International License, which permits use, sharing, adaptation, distribution and reproduction in any medium or format, as long as you give appropriate credit to the original author(s) and the source, provide a link to the Creative Commons licence, and indicate if changes were made. The images or other third party material in this article are included in the article's Creative Commons licence, unless indicated otherwise in a credit line to the material. If material is not included in the article's Creative Commons licence and your intended use is not permitted by statutory regulation or exceeds the permitted use, you will need to obtain permission directly from the copyright holder. To view a copy of this licence, visit <http://creativecommons.org/licenses/by/4.0/>.

## References

- Dowling L, Kennedy J, O’Shaughnessy S, Trimble D (2020) A review of critical repeatability and reproducibility issues in powder bed fusion. *Mater Des* 186:108346. <https://doi.org/10.1016/j.matdes.2019.108346>
- Salzbrenner BC, Rodelas JM, Madison JD, Jared BH, Swiler LP, Shen Y, Boyce BL (2017) High-throughput stochastic tensile performance of additively manufactured stainless steel. *J Mater Process Tech* 241:1–12. <https://doi.org/10.1016/j.jmatprotec.2016.10.023>
- Liu D, Wang Y (2019) Mesoscale multi-physics simulation of rapid solidification of Ti-6Al-4V alloy. *Addit Manuf* 25:551–562. <https://doi.org/10.1016/j.addma.2018.12.005>
- Promoppatum P, Yao SC (2019) Analytical evaluation of defect generation for selective laser melting of metals. *Int J Adv Manuf Technol*. <https://doi.org/10.1007/s00170-019-03500-z>
- Cunningham R, Zhao C, Parab N, Kantzos C, Pauza J, Fezzaa K, Sun T, Rollett AD (2019) Keyhole threshold and morphology in laser melting revealed by ultrahigh-speed X-ray imaging. *Science* (80–). 363:849–852. <https://doi.org/10.1126/science.aav4687>
- Dilip JJS, Zhang S, Teng C, Zeng K, Robinson C, Pal D, Stucker B (2017) Influence of processing parameters on the evolution of melt pool, porosity, and microstructures in Ti-6Al-4V alloy parts fabricated by selective laser melting. *Prog Addit Manuf* 2:157–167. <https://doi.org/10.1007/s40964-017-0030-2>
- Kruth JP, Froyen L, Van Vaerenbergh J, Mercelis P, Rombouts M, Lauwers B (2004) Selective laser melting of iron-based powder. *J Mater Process Technol* 149:616–622. <https://doi.org/10.1016/j.jmatprotec.2003.11.051>
- Song B, Dong S, Liu Q, Liao H, Coddet C (2014) Microstructure and tensile properties of iron parts fabricated by selective laser melting. *Mater Des* 54:727–733. <https://doi.org/10.1016/j.matdes.2013.08.085>
- Yadroitsev I, Smurov I (2010) Selective laser melting technology: From the single laser melted track stability to 3D parts of complex shape. *Phys Procedia* 5:551–560. <https://doi.org/10.1016/j.phpro.2010.08.083>
- Meier H, Haberland C (2008) Experimental studies on selective laser melting of metallic parts. *Materwiss Werkstsch* 39:665–670. <https://doi.org/10.1002/mawe.200800327>
- Snow Z, Nassar AR, Reutzel EW (2020) Invited Review Article: Review of the formation and impact of flaws in powder bed fusion additive manufacturing. *Addit Manuf* 36:101457. <https://doi.org/10.1016/j.addma.2020.101457>
- Sun Z, Tan X, Tor SB, Yeong WY (2016) Selective laser melting of stainless steel 316L with low porosity and high build rates. *Mater Des* 104:197–204. <https://doi.org/10.1016/j.matdes.2016.05.035>
- Clijsters S, Craeghs T, Buls S, Kempen K, Kruth JP (2014) In situ quality control of the selective laser melting process using a high-speed, real-time melt pool monitoring system. *Int J Adv Manuf Technol*. <https://doi.org/10.1007/s00170-014-6214-8>
- Yadroitsev I, Krakhmalev P, Yadroitsava I, Johansson S, Smurov I (2013) Energy input effect on morphology and microstructure of selective laser melting single track from metallic powder. *J Mater Process Technol* 213:606–613. <https://doi.org/10.1016/j.jmatprotec.2012.11.014>
- Gu D, Shen Y (2009) Balling phenomena in direct laser sintering of stainless steel powder: Metallurgical mechanisms and control methods. *Mater Des* 30:2903–2910. <https://doi.org/10.1016/j.matdes.2009.01.013>
- Cacace S, Semeraro Q (2018) About fluence and process parameters on maraging steel processed by selective laser melting: do they convey the same information? *Int J Precis Eng Manuf* 19:1873–1884. <https://doi.org/10.1007/s12541-018-0204-y>
- Cacace S, Semeraro Q (2021) Improvement of SLM build rate of A357 alloy by optimizing fluence. *J Manuf Process* 66:115–124. <https://doi.org/10.1016/j.jmapro.2021.03.043>
- Carlton HD, Haboub A, Gallegos GF, Parkinson DY, MacDowell AA (2016) Damage evolution and failure mechanisms in additively manufactured stainless steel. *Mater Sci Eng A* 651:406–414. <https://doi.org/10.1016/j.msea.2015.10.073>
- Voisin T, Calta NP, Khairallah SA, Forien J-B, Balogh L, Cunningham RW, Rollett AD, Wang YM (2018) Defects-dictated tensile properties of selective laser melted Ti-6Al-4V. *Mater Des* 158:113–126. <https://doi.org/10.1016/j.matdes.2018.08.004>
- Zhou X, Wang D, Liu X, Zhang DD, Qu S, Ma J, London G, Shen Z, Liu W (2015) 3D-imaging of selective laser melting defects in a Co-Cr-Mo alloy by synchrotron radiation micro-CT. *Acta Mater* 98:1–16. <https://doi.org/10.1016/j.actamat.2015.07.014>
- Kasperovich G, Haubrich J, Gussone J, Requena G (2016) Correlation between porosity and processing parameters in TiAl6V4

- produced by selective laser melting. *Mater Des* 105:160–170. <https://doi.org/10.1016/j.matdes.2016.05.070>
22. Stern F, Tenkamp J, Walther F (2020) Non-destructive characterization of process-induced defects and their effect on the fatigue behavior of austenitic steel 316L made by laser-powder bed fusion. *Prog Addit Manuf* 5:287–294. <https://doi.org/10.1007/s40964-019-00105-6>
  23. Kim FH, Moylan SP, Garboczi EJ, Slotwinski JA (2017) Investigation of pore structure in cobalt chrome additively manufactured parts using X-ray computed tomography and three-dimensional image analysis. *Addit Manuf* 17:23–38. <https://doi.org/10.1016/j.addma.2017.06.011>
  24. Yang T, Liu T, Liao W, MacDonald E, Wei H, Zhang C, Chen X, Zhang K (2020) Laser powder bed fusion of AISi10Mg: Influence of energy intensities on spatter and porosity evolution, microstructure and mechanical properties. *J Alloys Compd* 849:156300. <https://doi.org/10.1016/j.jallcom.2020.156300>
  25. Salarian M, Asgari H, Vlasea M (2020) Pore space characteristics and corresponding effect on tensile properties of Inconel 625 fabricated via laser powder bed fusion. *Mater Sci Eng A* 769:138525. <https://doi.org/10.1016/j.msea.2019.138525>
  26. Zhang Y, Zheng J, Xia Y, Shou H, Tan W, Han W (2020) A Porosity quantification for ductility prediction in high-pressure die casting AM60 alloy using 3D X-ray tomography. *Mater Sci Eng A* 772:138781. <https://doi.org/10.1016/j.msea.2019.138781>
  27. Erickson JM, Rahman A, Spear AD (2020) A void descriptor function to uniquely characterize pore networks and predict ductile-metal failure properties. *Int J Fract* 225:47–67. <https://doi.org/10.1007/s10704-020-00463-1>
  28. Spierings M, Schneider R, Eggenberger R (2011) Comparison of density measurement techniques for additive manufactured metallic parts. *Rapid Prototyp J* 17:380–386. <https://doi.org/10.1108/135525411111156504>
  29. David Legland (2020). *geom3d* (<https://www.mathworks.com/matlabcentral/fileexchange/24484-geom3d>), MATLAB Central File Exchange. Retrieved September 14, *geom3d*, (n.d.)
  30. Dinda SK, Warnett JM, Williams MA, Roy GG, Srirangam P (2016) 3D imaging and quantification of porosity in electron beam welded dissimilar steel to Fe-Al alloy joints by X-ray tomography. *Mater Des* 96:224–231. <https://doi.org/10.1016/j.matdes.2016.02.010>
  31. Chawla N, Deng X (2005) Microstructure and mechanical behavior of porous sintered steels. *Mater Sci Eng A* 390:98–112. <https://doi.org/10.1016/j.msea.2004.08.046>
  32. Biswal R, Syed AK, Zhang X (2018) Assessment of the effect of isolated porosity defects on the fatigue performance of additive manufactured titanium alloy. *Addit Manuf* 23:433–442. <https://doi.org/10.1016/j.addma.2018.08.024>
  33. Lavery NP, Cherry J, Mehmood S, Davies H, Girling B, Sackett E, Brown SGR, Sienz J (2017) Effects of hot isostatic pressing on the elastic modulus and tensile properties of 316L parts made by powder bed laser fusion. *Mater Sci Eng A* 693:186–213. <https://doi.org/10.1016/j.msea.2017.03.100>
  34. Suryawanshi J, Prashanth KG, Ramamurty U (2017) Mechanical behavior of selective laser melted 316L stainless steel. *Mater Sci Eng A* 696:113–121. <https://doi.org/10.1016/j.msea.2017.04.058>
  35. Kurzynowski T, Gruber K, Stopyra W, Kuźnicka B, Chlebus E (2018) Correlation between process parameters, microstructure and properties of 316 L stainless steel processed by selective laser melting. *Mater Sci Eng A*. <https://doi.org/10.1016/j.msea.2018.01.103>
  36. Rosenthal D (1941) Mathematical theory of heat distribution during welding and cutting. *Weld J* 20:220–234
  37. Boyce BL, Salzbrenner BC, Rodelas JM, Swiler LP, Madison JD, Jared BH, Shen YL (2017) Extreme-value statistics reveal rare failure-critical defects in additive manufacturing. *Adv Eng Mater*. <https://doi.org/10.1002/adem.201700102>
  38. Maskery I, Aboulkhair NT, Corfield MR, Tuck C, Clare AT, Leach RK, Wildman RD, Ashcroft IA, Hague RJM (2016) Quantification and characterisation of porosity in selectively laser melted Al-Si10-Mg using X-ray computed tomography. *Mater Charact* 111:193–204. <https://doi.org/10.1016/j.matchar.2015.12.001>

**Publisher's Note** Springer Nature remains neutral with regard to jurisdictional claims in published maps and institutional affiliations.